





One size fits all: Insights on Extrinsic Thermal Absorption from Similarity of Supernova Remnant Radio Continuum Spectra

Mario G. Abadi^{1,2} , Gabriela Castelletti³ , Leonardo Supan³ , Namir E. Kassim⁴ , and Joseph W. Lazio⁵

¹ CONICET-Universidad Nacional de Córdoba, Instituto de Astronomía Teórica y Experimental (IATE), Laprida 854, X5000BGR, Córdoba, Argentina

² Observatorio Astronómico, Universidad Nacional de Córdoba, Laprida 854, X5000BGR, Córdoba, Argentina

³ Instituto de Astronomía y Física del Espacio (IAFE), Ciudad Universitaria - Pabellón 2, Intendente Güiraldes 2160 (C1428EGA), Ciudad Autónoma de Buenos Aires - Argentina

⁴ Remote Sensing Division, Naval Research Laboratory, Code 7213, 4555 Overlook Ave SW, Washington, DC, 20375, USA

⁵ Jet Propulsion Laboratory, California Institute of Technology, Pasadena, CA 91106, USA

Received May XX, 2023; accepted Month XX, 2023

ABSTRACT

Typically, integrated radio frequency continuum spectra of supernova remnants (SNRs) exhibit a power-law form due to their synchrotron emission. In numerous cases, these spectra show an exponential turnover, long assumed due to thermal free-free absorption in the interstellar medium. We use a compilation of Galactic radio continuum SNR spectra, with and without turnovers, to constrain the distribution of the absorbing ionized gas. We introduce a novel parameterization of SNR spectra in terms of a characteristic frequency ν_* , which depends both on the absorption turnover frequency and the power-law slope. Normalizing to ν_* and to the corresponding flux density, S_* , we demonstrate that the stacked spectra of our sample reveal a similarity in behavior with low scatter (r.m.s. $\sim 15\%$), and a unique exponential drop-off fully consistent with the predictions of a free-free absorption process. Observed SNRs, whether exhibiting spectral turnovers or not, appear to be spatially well mixed in the Galaxy without any evident segregation between them. Moreover, their Galactic distribution does not show a correlation with general properties such as heliocentric distance or Galactic longitude, as might have been expected if the absorption were due to a continuous distribution of ionized gas. However, it naturally arises if the absorbers are discretely distributed, as suggested by early low-frequency observations. Modeling based on H II regions tracking Galactic spiral arms successfully reproduces the patchy absorption observed to date. While more extensive statistical datasets should yield more precise spatial models of the absorbing gas distribution, our present conclusion regarding its inhomogeneity will remain robust.

Key words. ISM: supernova remnants; ISM: H II regions, radio continuum: general; radio continuum: ISM

1. Introduction

Continuum radio emission from shell-type supernova remnants (SNRs) is due to synchrotron emission from relativistic electrons spiraling in compressed circumstellar and interstellar magnetic fields, inferred to be a major source of Galactic cosmic ray electrons. Their intrinsic nonthermal continuum spectra typically reflect a power-law dependence of the flux density on the frequency, $S \propto \nu^\alpha$, the spectral slope of which is shaped by particle acceleration processes associated with their blast wave. Both, linear and nonlinear diffusive shock acceleration models have been proposed to explain the production of the energetic particles and the synchrotron emission (see e.g., Blandford & Eichler 1987, Malkov & Drury 2001 for reviews).

Free-free thermal absorption from either internal or external ionized gas can impact the integrated radio spectra of SNRs by causing turnovers at the lowest frequencies ($\nu < 100$ MHz). In the former case, for shell-type SNRs the absorption is concentrated near the center of the remnant. It is caused by the ionization of cool, unshocked ejecta lying interior to the reverse shock and ionized by its X-ray emission. It has been detected in the bright, young SNRs Cas A (Kassim et al. 1995; DeLaney et al. 2014; Arias et al. 2018) and Tycho (Arias et al. 2019). Hints

of interior absorption attributed to its thermal filaments has also been discerned in the Crab nebula (Bietenholz et al. 1997). These special cases of interior or *intrinsic* thermal absorption in young SNRs remain observationally rare and will no longer be considered in this paper.

The much more common source of turnovers in SNR continuum spectra is exterior or *extrinsic* absorption from ionized gas outside the main boundaries of the remnant and located anywhere along the line of sight. Although it is customary to distinguish two different cases, local and non-local, the spectra by themselves do not give any information about the distance between the emitter and the absorber. The local case can occur near the periphery of the SNR as the blast wave interacts with the surrounding interstellar medium (ISM) or from foreground H II regions within the same complex. On the other hand, the non-local case refers to absorption by unrelated more distant ionized gas. Evidence for spectral turnovers under 100 MHz with thermal absorption signatures dates to the classic works of Dulk & Slee (1972, 1975) and Kassim (1989), but were significantly limited due to poor angular resolution imposed by the Earth's ionosphere on instruments at the time. Kassim (1989) suggested at least some absorption occurs non-locally in extended (~ 100 pc), low-density envelopes (EHEs) associated with normal Galactic H II regions along the line of sight. EHEs had been inferred

* E-mail: mario.abadi@unc.edu.ar

earlier from widespread so-called Galactic ridge recombination lines detected at meter wavelengths (325 MHz) (Anantharamiah 1985).

Synchrotron emission combined with thermal absorption produce integrated radio continuum spectra for most Galactic SNRs that can be fit by a power-law plus an exponential turnover at low frequencies ($\nu < 100$ MHz). Turnover spectra offer crucial insights into the ionized gas properties of the absorbers in our Galaxy. In particular, the presence and locations of SNRs with turnover spectra, or limits implied by those without turnovers at currently accessible frequencies, offer unique constraints on the spatial distribution of this gas, improving our understanding of the interstellar medium. However, the use of different reference frequencies (ν_0) to parameterize the optical depth (τ_0) associated with these turnovers has made it awkward to compare spectra from different SNRs and formulate a clear picture of the underlying absorbing ionized medium. Therefore, in order to make the comparison of optical depths easier and ensure comparability between published values, it is beneficial to convert all values to a common reference frequency. To address this issue, we propose an alternative parameterization of turnover spectra that avoids the need for multiple reference frequencies, streamlining the analysis and facilitating the comparison of different SNR samples.

Early sub-arcminute resolution imaging below 100 MHz of SNRs W49B (Lacey et al. 2001) and 3C 391 (Brogan et al. 2005) began resolving thermal absorption towards SNRs. They foreshadowed emerging arc-second resolution, mJy sensitivity capabilities to expand thermal absorption studies to a larger population of sources for constraining the ionized gas, diagnosing direct interactions, and constraining the relative radial superposition of emitters and absorbers. More recently, Castelletti et al. (2021) significantly expanded the sample, by performing a detailed analysis of 9 SNRs showing turnovers on the basis of radio, infrared, and molecular data. Four of these have been attributed to the discrete but non-local extrinsic scenario proposed by Kassim (1989) (see "Absorption from extended envelopes of normal H II regions (EHEs)" in their Table 3). The remaining 5 are far better explained by local extrinsic absorption by foreground ionized gas in the SNR neighbourhood (see "Absorption: Special cases" in their Table 3). Comparing these two tables, the main parameter distinguishing between the non-local and local extrinsic scenarios seems to be the best-fit free-free optical depth τ_0 (at a reference frequency $\nu_0=74$ MHz) in the integrated continuum spectra: a low one, $\tau_0 \sim 0.1$, for the case of external H II regions versus a high one, $\tau_0 \sim 1$, in the case of local H II regions or interactions at the ionised interface between SNR blast wave with their host complex. The only exception seems to be G39.2-0.3 (3C 396), which has a low $\tau_0 \sim 0.063$ but is classified as local rather than non-local absorption. Additionally, best-fit models including measurements in the low frequency portion of the spectrum are reported in Kovalenko et al. (1994b), and Kassim (1989).

Here we explore whether sufficient "trees" now exist to begin visualizing the "forest". Is it possible to use the properties of the observed (or inferred) turnovers, coupled with improving knowledge of SNR distances and H II region distributions, to constrain the spatial distribution of the absorbers? We hope posing this question here can stimulate forthcoming statistical and targeted studies of the seemingly ubiquitous phenomena of thermal absorption towards Galactic SNRs at low frequencies. The organization of this paper is as follows. Section 2 describes our sample of integrated SNR radio continuum spectra with or without turnovers at low frequencies. Section 3 presents our analysis

of all spectra in context of external thermal absorption. In Sect. 4 we present our simple Galactic distribution model for absorption of SNR emission. The main results and future work are summarized in Sect. 5.

2. Data collection

Our analysis is based on 129 integrated SNR radio continuum spectra. Among them, 57 exhibit a turnover at frequencies below 100 MHz, while the remaining 72 are well fit by simple power law spectra. The former group includes 9 SNR spectra taken from Castelletti et al. (2021), 3 constructed for this paper, 31 from Kovalenko et al. (1994b), and 14 from Kassim (1989) (see Table A.1; note that certain sources appear in more than one reference). The group with pure power law spectra comprise 2 sources from Castelletti et al. (2021), 15 remnants whose spectra were constructed for this work, 45 from Kovalenko et al. (1994b), and 10 from Kassim (1989) (for reference see the labels in Figs. 4, 5, and 6).

While constructing the spectra for this study, encompassing both those with and without turnovers, our main goal was to minimize the typical scatter at the lower frequencies. To achieve this, we conducted new flux density measurements using available images from two resources: the Very Large Array Low-Frequency Sky Survey Redux (VLSSr, at 74 MHz, resolution 75''; Lane et al. 2004) and the Galactic and Extragalactic All-sky Murchison Widefield Array survey (GLEAM, at 88, 118, 155, and 200 MHz, resolutions from $\sim 6'$ to $\sim 2'$ Hurley-Walker et al. 2019). These fluxes are critical for constraining the low-frequency portion of the spectra, which for many years have remained problematic due to the relatively poor angular resolution and sensitivity of legacy instruments, such as Culgoora (80 MHz, Slee & Higgins 1973, 1975; Slee 1977), Clark Lake TPT (30.9 MHz, Kassim 1988), and the Pushchino telescopes (83 MHz, Kovalenko et al. 1994a).¹ It is worth noting that at the time of our analysis, no images below 100 MHz were available for the SNRs in our sample from surveys conducted with modern instruments like the LOw Frequency ARray (LOFAR) or the Long Wavelength Array (LWA). At higher frequencies, depending on the position of the SNR in the sky, the spectra incorporate new flux density measurements from the Southern Galactic Plane Survey (SGPS, McClure-Griffiths et al. 2005) at 1420 MHz, the S-band Polarisation All Sky Survey (S-PASS, Carretti et al. 2019) at 2303 MHz, and the Parkes 6 cm survey at 5000 MHz (Haynes et al. 1978). All our new flux estimates have been combined with previous measurements from the literature. The criteria adopted for collecting the data for the new spectra are consistent with those reported in Castelletti et al. (2021). This includes encompassing only measurements with error estimates less than 30%, ensuring there are no significant deviations from the best-fit model, using interferometer data that adequately recover short spacings information at frequencies above 1000 MHz, and single-dish data with appropriate resolution to prevent flux density overestimates due to high confusion levels. In total, considering the spectra from Castelletti et al. (2021) and those constructed for this work, we have collected around 570 flux density measurements. The improvements in the accuracy

¹ Additional flux density measurements below 100 MHz, which were included in our spectral analysis and obtained from the literature, are as follows: 10 MHz Bridle & Purton (1968), 19 MHz Rishbeth (1958), 10-25 MHz Braude et al. (1969, 1979), 22 MHz Roger et al. (1969, 1986), 26 MHz Erickson & Cronyn (1965); Viner & Erickson (1975), 29.9 MHz Jones & Finlay (1974), 38 MHz Williams et al. (1966), and 86 MHz Mills & Slee (1957); Mills et al. (1958, 1960).

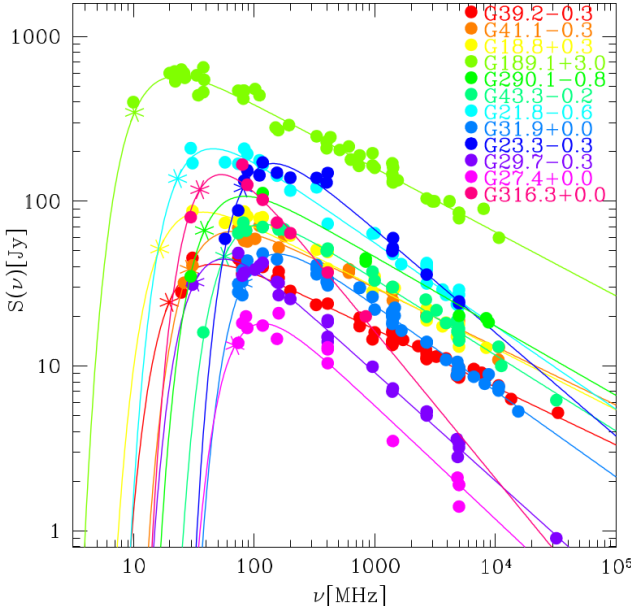


Fig. 1. Radio flux density measurements (colored filled circles) as a function of frequency for 12 SNRs spectra with turnovers (see labels). This sample is build up by 9 SNR spectra reported in Castelletti et al. (2021) plus 3 new spectra for the SNRs G189.1+3.0, G290.1-0.8, and G316.3+0.0, which were specifically constructed for this work. The solid colored lines shows each corresponding best fit given by Eq. 2 with parameters included in our Table A.1. The asterisk symbol indicates the individual characteristic frequency ν_* .

of the radio spectral index determinations for the SNRs in our sample are about one order of magnitude when compared to previously published estimates.

3. Analysis

SNRs that exhibit thermal turnovers are typically characterized by fitting the integrated continuum flux density $S(\nu)$ at a frequency ν using a power-law plus exponential cutoff equation:

$$S(\nu) = S_0 \left(\frac{\nu}{\nu_0} \right)^\alpha \exp \left[-\tau_0 \left(\frac{\nu}{\nu_0} \right)^{-2.1} \right], \quad (1)$$

where α is the power-law spectral index, S_0 is a flux density normalization, and τ_0 is the free-free optical depth, both measured at a reference frequency ν_0 . The power-law term in this equation reflects the intrinsic synchrotron emission of the SNR, while the exponential term accounts for absorption due to ionized gas along the line of sight. However, because authors adopt different reference frequencies, typically related to their specific observing frequencies, it is often necessary to apply the scaling: $\nu'_0/\nu_0 = (\tau_0/\tau'_0)^{1/2.1}$ and $S'_0/S_0 = (\nu'_0/\nu_0)^\alpha$ where primed variables correspond to a reference frequency ν'_0 . Some authors (e.g., Castelletti et al. 2021) use the same reference frequency ($\nu_0 = 74$ MHz) for both physical process, i.e. in the power-law and in the exponential; others (e.g., Kassim 1989) present their data using two different reference frequencies, one for the emission $\nu_0 = 408$ MHz and one for the absorption $\nu_0 = 30.9$ MHz. Moreover, others (e.g., Kovalenko et al. 1994b) use a unique reference frequency for absorption $\nu_0 = 100$ MHz but different ones for each individual SNR emission over a broad range from $\nu_0 = 175$ MHz to $\nu_0 = 6000$ MHz (see Table A.1). Although it is straightforward to convert values from one frequency to the other, the discordant parametrization can confuse comparison.

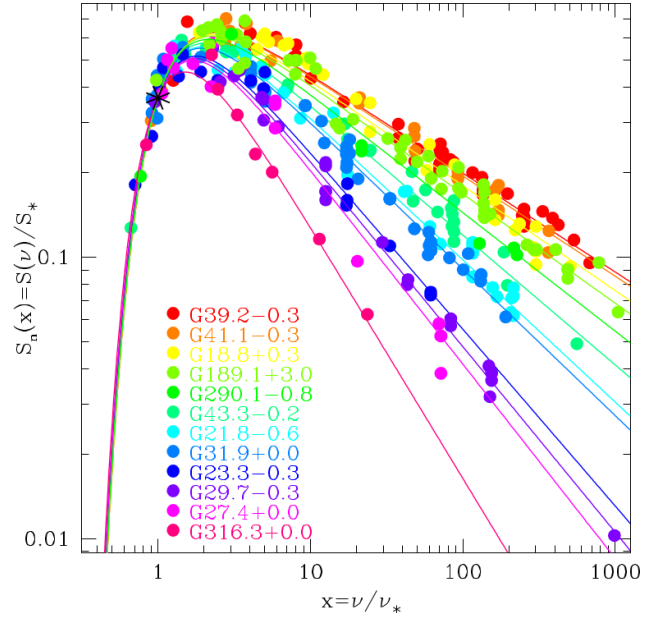


Fig. 2. Normalized radio flux density $S_n(x) = S(\nu)/S_* = x^\alpha \exp(-x^{-2.1})$ measurements (colored filled circles) as a function of the normalized frequency $x = \nu/\nu_*$ for 12 SNRs spectra with turnover (see labels). This sample comprises 9 SNR spectra reported in Castelletti et al. (2021), with the addition of 3 new spectra for the SNRs G189.1+3.0, G290.1-0.8, and G316.3+0.0 included for this work. Solid lines show their corresponding fit with parameters presented in our Table A.1. This normalized form sorts SNRs spectra in increasing order according to their slope from bottom $\alpha = -0.89$ to top $\alpha = -0.35$. The black asterisk symbol marks the characteristic frequency ν_* and highlight how the normalization is done.

To avoid such complications we re-write Eq. 1 independent of the reference frequency as:

$$S(\nu) = S_* \left(\frac{\nu}{\nu_*} \right)^\alpha \exp \left[-\left(\frac{\nu}{\nu_*} \right)^{-2.1} \right], \quad (2)$$

where ν_* is a characteristic frequency and S_* is a characteristic flux density. Equation 2 is identical to Eq. 1 but expressed by removing the explicit dependency of ν_0 , τ_0 , and S_0 , i.e., independent of the adopted reference frequency ν_0 . Notice that $\nu_* = \tau_0^{1/2.1} \nu_0$ and $S_* = S_0 (\nu_*/\nu_0)^\alpha$. Computing these characteristic parameters using any other reference frequency gives the same values of ν_* and S_* . Moreover, the physical meaning of these two parameters is straightforward: ν_* is related to the position of the turnover frequency ν_{to} , i.e., where $S(\nu)$ has its maximum, and S_* is the spectrum normalization height. The turnover frequency can be computed by deriving the flux density and equalizing it to zero to yield $\nu_{to}/\nu_* = (-2.1/\alpha)^{1/2.1}$. Then, the characteristic frequency ν_* is determined by both the turnover frequency ν_{to} and the power-law slope α . Only in the critical case where $\alpha = -2.1$ we have $\nu_* = \nu_{to}$ while for $\alpha > (<) -2.1$, we have $\nu_* < (>) \nu_{to}$. For a fiducial value of $\alpha \sim -0.5$ we obtain $\nu_* \sim \nu_{to}/2$, while for typical values of SNRs power-law slopes $-0.89 \lesssim \alpha \lesssim -0.35$ (see Table A.1) we have $1.5 \lesssim \nu_{to}/\nu_* \lesssim 2.5$. It is worth noting that while Eq. 1 has been widely adopted by many authors, to the best of our knowledge, the simple parametrization given by Eq. 2 has not been proposed before. An additional advantage of this parametrization in terms of ν_* is that low values of ν_* indicate low ν_{to} or lower frequency turnovers, while high ν_* indicate high ν_{to} with absorption commencing at higher frequencies.

To illustrate our approach to constrain the properties of the absorbing gas, in the next two subsections we apply these ideas

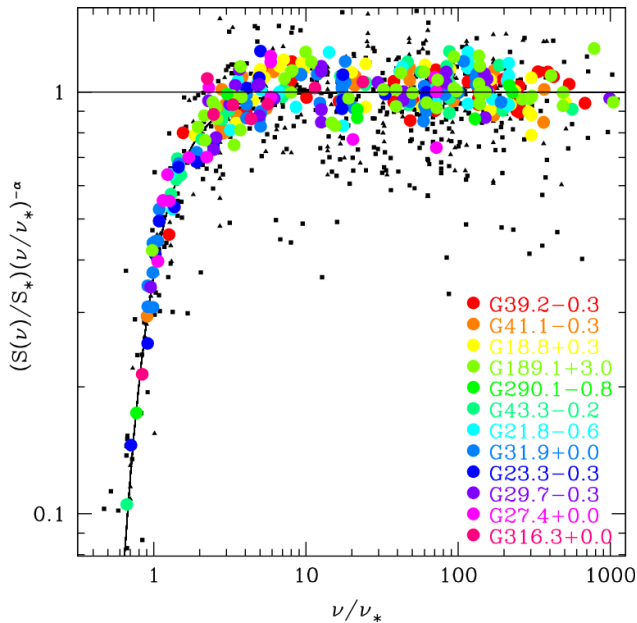


Fig. 3. Normalized radio flux density measurement as a function of frequency for 9 SNR spectra presented in Castelletti et al. (2021) plus 3 new spectra for the SNRs G189.1+3.0, G290.1-0.8, and G316.3+0.0, constructed for this work (colored filled circles), along with data from Kovalenko et al. (1994b) (black filled squares) and Kassim (1989) (black filled triangles). In order to highlight the drop-off behavior, the data are normalized to the power-law emission $E(x) = x^\alpha$, where $x = \nu/\nu_*$. The curved solid line is the normalized absorption $A(x) = \exp(-x^{-2.1})$. The total r.m.s. of the colored circles is less than 11%. At $\nu \sim 2.75\nu_*$ approximately 50% of the emission is absorbed.

to a sample of 129 SNRs spectra with and without observed turnovers. For the latter group, we utilize upper limits for ν_* based on the lowest frequency measured.

3.1. SNRs with spectral turnovers

In Fig. 1 we display the measurements of 12 SNRs with turnovers, 9 of them reported by Castelletti et al. (2021) plus 3 constructed for this work. Accordingly, Fig. 1 illustrates the complex superposition of spectra reflecting the relatively large range in spectral index ($-0.89 \leq \alpha \leq -0.35$) and optical depth ($0.016 \leq \tau_0 \leq 1.21$ at $\nu_0 = 74$ MHz) listed in Table A.1.

In Fig. 2 we show the first advantage of the new parametrization offered through Eq. 2. Here, we plot the normalized flux density $S_n(x) = S(\nu)/S_*$ as a function of the normalized frequency $x = \nu/\nu_*$ for the same 12 SNRs plotted in Fig. 1. The dynamic range of ~ 700 in $S(\nu)$ seen in Fig. 1 is reduced by at least a factor ~ 10 using the normalized form also showing a significantly smaller scatter. Moreover, the observational data at low frequencies, i.e. lower than the characteristic frequency $\nu < \nu_*$ of the 12 SNRs when stacked together, are well fit by a unique drop off curve $A(x) = \exp(-x^{-2.1})$ that is more clearly traced than in the individual curves. At high frequencies, i.e. higher than the characteristic frequency $\nu > \nu_*$, the solid curves differ only due to their slopes α . Power-law emissions are ordered by their slope from a steep $\alpha = -0.89$ value for G316.3+0.0 (bright pink filled circles and solid curve) to a flat $\alpha = -0.35$ for G39.2-0.3 (red filled circles and solid curve).

In Fig. 3 we applied an additional normalization step by dividing the flux density $S_n(x)$ by the power-law emission factor of each SNR, $E(x) = x^\alpha$. Another advantage of the new normal-

ization is that any SNR spectrum can be fit by a unique absorption equation $A(x) = \exp(-x^{-2.1})$, as depicted by the solid black curve. A reduced r.m.s. scatter of $\sim 11\%$ is apparent for these 12 SNRs stacked together indicating the quality of the fits. To enlarge our sample, we have also compiled spectra with a low-frequency turnover of 14 SNRs reported in Kassim (1989) and 31 from Kovalenko et al. (1994b). These dataset are represented by filled small black squares and triangles, respectively. The inclusion of these two additional samples reinforces our results showing a similar trend, albeit with a higher r.m.s. scatter.

3.2. Pure power-law SNRs spectra

Pure power-law spectra can be interpreted as absorbed spectra as well, but absorbed at such low frequencies that the turnover has not been observationally detected yet. For example, if the turnover frequency is at $\nu_* = 30$ MHz, but there are no quality measurements at comparable frequencies, the spectrum is usually fit by a pure power-law. Indeed, if a turnover has not been detected, the lowest measured frequency ν_{low} of a spectrum can be considered as an upper limit for the undetected turnover frequency. We therefore expanded our sample of turnover spectra by assigning a turnover to the pure power law fits, allowing a maximum of a 10% difference between the extrapolated power-law and the absorbed fit at the lowest frequency. Using Eq. 2, we have $\nu_* = \nu_{\text{low}}(\log f)^{1/2.1}$ where f is a parameter that fixes the ratio between the flux density power-law and the turnover fit at ν_{low} . We have adopted a value of $f = 1.1$, which means that the difference is 10% yielding $\nu_* \sim 0.33\nu_{\text{low}}$.

Figs. 4, 5, and 6 are analogous to Figs. 1, 2, and 3, respectively, but constructed for SNRs whose integrated radio continuum spectra are fitted by pure power laws. Two of the plotted spectra are taken from Castelletti et al. (2021), and the other 15 were constructed for this work as explained in Sect. 2. In Fig. 4 colored solid lines are the corresponding pure power-law best fit to the data points of each SNR, while dotted lines are the putative turnover spectra given by Eq. 2. The asterisk symbols indicate the maximum characteristic frequency ν_* allowed by the lowest frequency observed ν_{low} . Again, the large dynamic range in measured flux densities of ~ 300 is reduced by a factor ~ 7 when the normalized form is adopted (see Fig. 5). A final normalization to the individual power law slope α shows good quality fits with r.m.s. $\sim 15\%$ as seen in the colored open circles of Fig. 6. These fits are better quality than the pure power-law samples of Kovalenko et al. (1994b) and Kassim (1989) depicted by open small black squares and triangles, respectively.

3.3. Characteristic frequency ν_* distribution

In Fig. 7 we show as a filled histogram the distribution of ν_* values, computed for our three samples (Castelletti et al. (2021) plus this work, Kovalenko et al. (1994b), and Kassim (1989) listed in Table A.1) ranging from ~ 10 MHz to 100 MHz. In the upper panel, $\nu_* \sim 40$ MHz separates two populations with low ($\tau \sim 0.1$) and high ($\tau \sim 1$) optical depths reported in Table 3 of Castelletti et al. (2021); these two subsamples were labeled as “Absorption from extended envelopes” (non-local) and “Absorption: Special cases” (local), respectively. The classification was made by additional information obtained from low-frequency radio recombination lines, infrared fine-structure, and molecular line emission to distinguish between spectral turnovers attributed to ionized material in the ISM unrelated to the SNR (non-local) and an ionized component in the immediate SNR’s surroundings

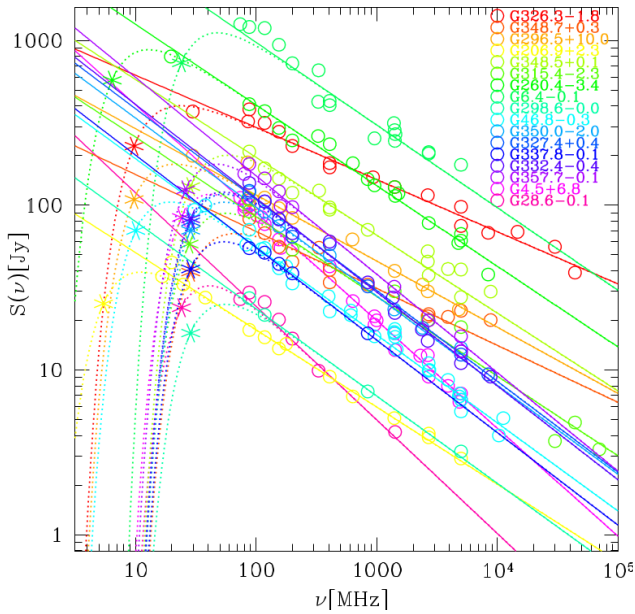


Fig. 4. Radio flux density measurements (colored open circles) as a function of frequency for 17 SNRs spectra without turnovers (see labels). This sample includes the spectra of G4.5+6.8 and G28.6–0.1 SNRs published in Castelletti et al. (2021) plus 15 new ones constructed for this work. The solid colored lines shows each corresponding power-law best fit while the dotted ones corresponds to Eq. 2 with a characteristic frequency ν_* (see asterisk symbol) assigned as an upper limit according to the lowest measured frequency ν_{low} .

(local). These low ($\nu_* \lesssim 40$ MHz) and high ($\nu_* \gtrsim 40$ MHz) populations might hint at non-local vs. local absorbers in the other two samples, Kassim (1989) and Kovalenko et al. (1994b), shown in the middle and bottom panels of Fig. 7. However, due to the incompleteness of our samples, it is not possible to definitively determine yet whether these populations represent truly distinct groups or merely the low and high tails of a single population with intrinsic dispersion. The open histograms show the characteristic frequency ν_* of power-law spectra assigned according to their observed lowest frequency ν_{low} . In the upper panel, the observed peak at $\nu_* \sim 30$ MHz is a direct consequence of the GLEAM survey cutoff frequency at $\nu_{\text{low}} \sim 88$ MHz (see asterisk symbols in Fig. 4). At $\nu_* \sim 10$ MHz we have measurements obtained at lower frequencies by the Clark Lake TPT (30.9 MHz), Culgoora (80 MHz), and Pushchino (83 MHz) telescopes (see Sect. 2).

Notice that the upper color bar indicates the color coding adopted in Fig. 8 and Fig. 9 based on $\log(\nu_*/\text{MHz})$ value instead of using the SNRs' names, as done in Fig. 1 through Fig. 6, as well as in Fig. 10 and Fig. 11. On the other hand, we have also searched for, and did not find, any significant correlations between the three fitted parameters S_* , ν_* , and α . This result indicates that the emission and absorption processes in our limited SNR sample are independent of each other. A useful and direct application of the characteristic frequency ν_* parametrization is the possibility to provide insights concerning the properties of the absorbing thermal gas. A complete mapping of the ν_* distribution in the Galaxy should offer strong and unique constraints on the distribution of the ionized absorbing gas. Despite the incomplete and non-uniform nature of current surveys on SNRs, we have utilized our compiled sample to extract fundamental and widespread characteristics from the presently available data. Additionally, we have compared our findings with ad-hoc constructed models in order to draw initial conclusions regarding the

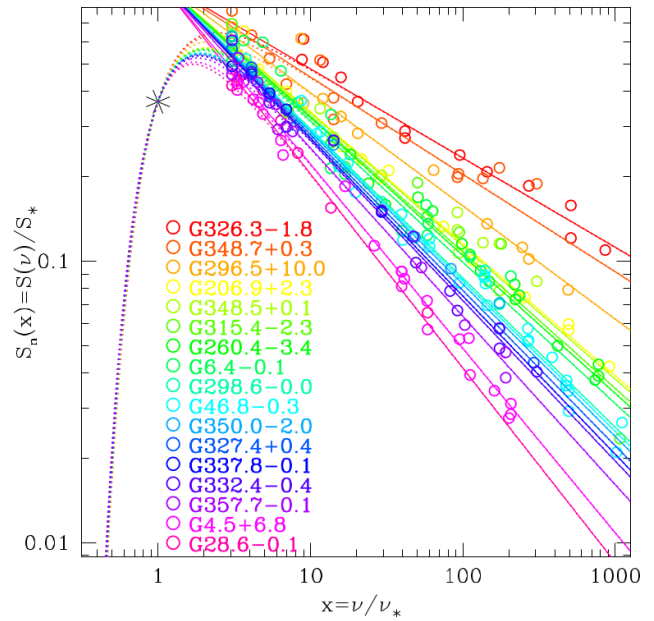


Fig. 5. Normalized radio flux density $S_n(x) = S(\nu)/S_* = x^\alpha \exp(-x^{-2.1})$ measurements (colored open circles) as a function of the normalized frequency $x = \nu/\nu_*$ for 17 SNRs spectra without low frequency turnover (see labels). This sample includes the spectra of G4.5+6.8 and G28.6–0.1 SNRs published in Castelletti et al. (2021) plus 15 new collected for this work. Extended lines show their power-law fit while dotted ones correspond to Eq. 2 with characteristic frequency ν_* (asterisk symbol) assigned as an upper limit according to the lowest measured frequency ν_{low} . This normalized form sorts SNRs spectra in increasing order according to their slope from bottom $\alpha = -0.69$ to top $\alpha = -0.32$. The black asterisk symbol marks the characteristic frequency ν_* and highlights how the normalization is done.

absorber population. In Fig. 8 we show the projected spatial distribution onto the Galactic plane for all the SNRs with turnovers (filled symbols) in our three samples. We have also included SNRs from Castelletti et al. (2021) plus this work, Kovalenko et al. (1994b), and Kassim (1989) whose spectra are well-fitted by a pure power-law (open symbols) colored according to their upper limit characteristic frequency assigned (see Sect. 3.2 and Fig. 4). At first glance, it does not appear that there is a significant segregation between SNRs with and without spectral turnovers, or an apparent gradient in ν_* with global properties like heliocentric distance or Galactic longitude. This qualitative result indicates that the absorbing media is probably made of discrete ionized regions rather than a continuous gas distribution. Likewise, the absence of spectral turnover in some distant SNRs, coupled with significant absorption in some nearby ones, was first interpreted by Kassim (1989) as a patchy distribution of low-frequency absorbing gas, and not caused by a broadly distributed component of the ISM. Here, we test this original idea by adding the spectra presented by Castelletti et al. (2021), those constructed for this work, along with those included in Kovalenko et al. (1994b).

To facilitate the interpretation of these observational findings, in the following section we developed a two-dimensional toy model that simulates the power-law emission from SNRs and takes into account the absorption caused by intervening ionizing gas.

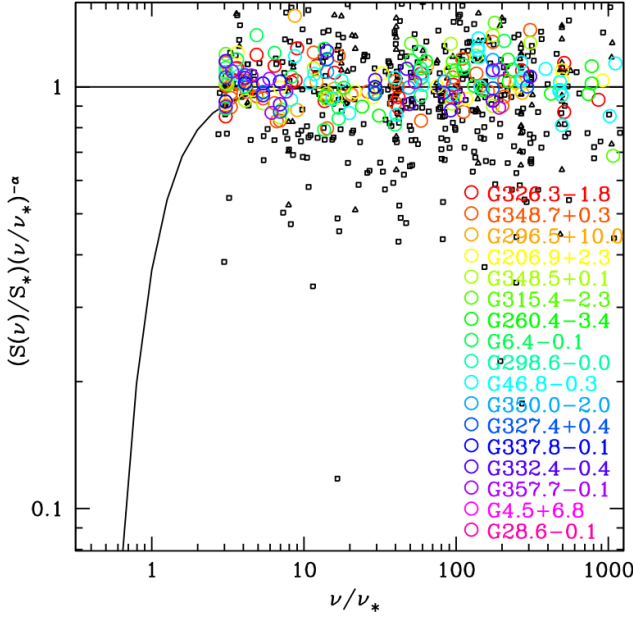


Fig. 6. Normalized radio flux density measurements as a function of frequency for the SNRs G4.5+6.8 and G28.6-0.1 presented in Castelletti et al. (2021) plus 15 new SNRs spectra constructed for this work (colored open circles). These datasets are complemented by flux density estimates from Kovalenko et al. (1994b) (black open squares) and Kassim (1989) (black open triangles). In order to highlight the drop-off behavior, the data are normalized to the power-law emission $E(x) = x^\alpha$, where $x = \nu/\nu_*$. The curved solid line is the normalized absorption $A(x) = \exp(-x^{-2.1})$. The total r.m.s. of the colored open circles is less than 15%.

4. Absorption Model

We assumed that the SNRs are distributed on the Galactic plane following an exponential surface number density profile: $\Sigma(R) = \Sigma_0 \exp(-R/R_d)$, where Σ_0 is the central surface density and R_d is the scale-length. We tied Σ_0 to a mock assumption of 20,000 SNRs sufficiently large to mimic the statistical behavior of a generic population of remnants distributed on the Galactic plane with $R_d = 3.5$ kpc following the Milky Way stellar scale-length. We started by attributing the absorption to ionized gas characterized by an emission measure (see Eq. 6 and discussion below) predicted by the continuum model NE2001, at fixed temperature (Cordes & Lazio 2002). We found that the NE2001 model predicts a correlation between absorption and distance, a correlation that is not observed. We attribute the discrepancy to the fact that the NE2001 model assumes a nearly continuous distribution of ionized gas, together with its reliance on measurements of relatively nearby pulsars (PSRs). Recognizing that H II regions are discrete structures, we then considered a model in which a set of discrete absorbing regions, representing H II regions or H II region complexes, are distributed throughout the disk of the Galaxy.

We place clumps of ionized gas preferentially along the Galactic spiral arms following the Hou & Han (2014) four-arm logarithmic model (see their Table 1). Clumps are circular with radius r drawn from a Maxwell-Boltzmann probability density distribution:

$$p(r) = \sqrt{\frac{2}{\pi}} \frac{r^2 \exp(-r^2/a^2)}{a^3}, \quad (3)$$

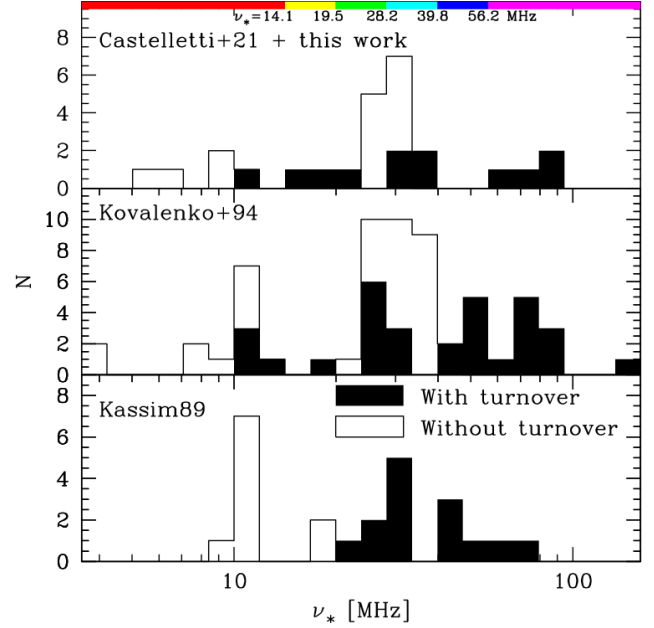


Fig. 7. Histograms showing the distribution of characteristic frequencies ν_* for the three samples analyzed here. Each panel corresponds to a different sample, as indicated by the labels. The filled histograms show the distribution of ν_* for SNRs spectra with turnovers, while the open ones depict the estimated upper limit of ν_* based on the lowest measured frequency ν_{low} for spectra without turnovers.

with a parameter $a = 50$ pc. Initially, we distribute homogeneously clumps along the spiral arms; then we add a random noise of 5% in their polar radius to mimic the fact that H II regions are not perfectly distributed along the spiral arms and also that the spiral arms themselves are not perfectly delineated in real galaxies. We also fix the number of absorbers in a way that the initial (i.e. before adding the random noise) mean separation between them is 5 times their typical size. All together these conditions result in 981 simulated H II regions that trace approximately the spiral arms and that they do not overlap each, consistent with the number and distribution of Galactic H II regions revealed by observational surveys that typically point out hundreds to thousands of these objects (Anderson et al. 2018; Wenger et al. 2021, and references therein).

The predicted characteristic frequency ν_* can be estimated using its definition, introduced in Sect. 3, $\nu_* = \tau_0^{1/2.1} \nu_0$ where the optical depth τ_0 can be computed from the physical properties of the absorbing ionized gas using the following equation (Wilson et al. 2009)

$$\tau_0 = 3.014 \times 10^{-2} \left(\frac{T_e}{\text{K}} \right)^{-3/2} \left(\frac{\nu_0}{\text{GHz}} \right)^{-2} g_{\text{ff}} \left(\frac{\text{EM}}{\text{pc cm}^{-6}} \right), \quad (4)$$

where T_e is the gas electron temperature,

$$g_{\text{ff}} = \ln \left[4.955 \times 10^{-2} \left(\frac{\nu_0}{\text{GHz}} \right)^{-1} \right] + 1.5 \ln \left(\frac{T_e}{\text{K}} \right) \quad (5)$$

is the Gaunt factor, and

$$\text{EM} = \int_0^L n_e^2 dx \quad (6)$$

is the emission measure depending on the electron density, n_e , integrated along the linear length, L , of the intervening medium. Assuming a constant electron density, the emission measure is

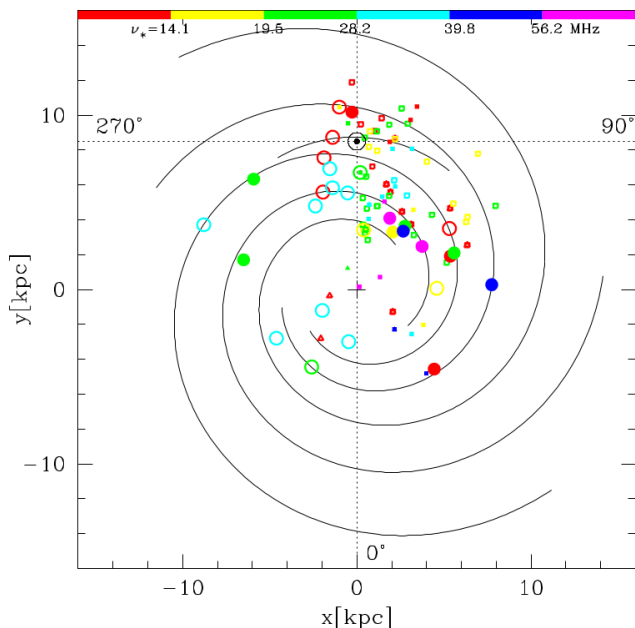


Fig. 8. Projected spatial distribution onto the Galactic plane of SNRs in the three samples analyzed here with distances taken from Ranasinghe & Leahy (2022) and colored according to $\log(v_*/\text{MHz})$ using the color bar code. Filled symbols show the location of SNRs with turnover spectra, while the open symbols indicate those sources not showing turnovers. Circles correspond to Castelletti et al. (2021) plus this work data, squares correspond to Kovalenko et al. (1994b), and triangles to Kassim (1989). As a guidance the solid black lines show the position of the spiral arms taken from the Hou & Han (2014) model. The central plus symbol indicates the position of the Galactic center, the solar symbol shows the Sun's position, and the dotted lines the Galactic quadrants. The colored points do not show any strong dependence on heliocentric distance or Galactic longitude (see Fig. 10 and 11).

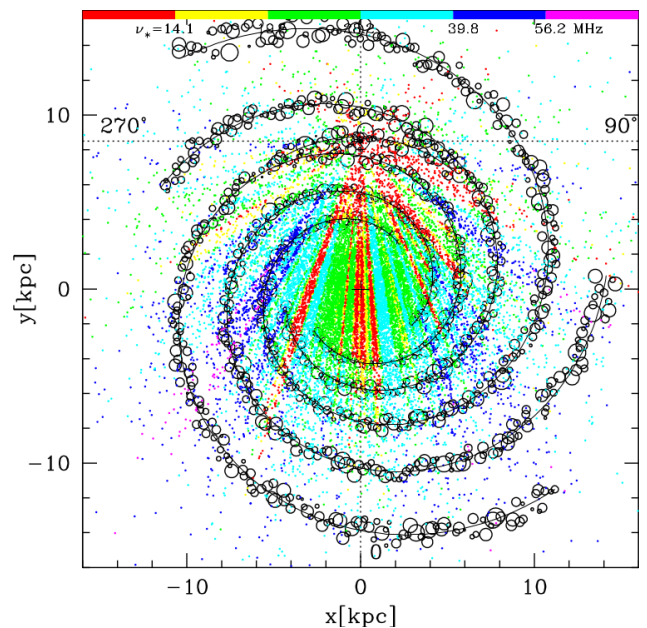


Fig. 9. Spatial distribution of an assumed mock sample of 20,000 SNRs (points colored by $\log(v_*/\text{MHz})$ using the color bar code). Absorbers (open circles) are distributed along the Galactic spiral arms taken from the Hou & Han (2014) model (solid black curves). Each absorber is assumed to have a constant low density $n_e = 2.0 \text{ cm}^{-3}$, a temperature $T_e = 5000 \text{ K}$, and radius r drawn from a Maxwell-Boltzmann probability density distribution with a median of 50 pc. The scale of each open circle has been expanded by an arbitrary factor 3 in order to make the plot more clear. The central plus symbol indicates the position of the Galactic center, the solar symbol shows the Sun's position, and the dotted lines the Galactic quadrants. The colored points do not show any strong dependence on heliocentric distance or Galactic longitude (see Fig. 10 and 11).

$\text{EM} = n_e^2 L$. Therefore, we have $v_* \sim n_e^{0.95} L^{0.47} / T_e^{0.71}$, i.e. the characteristic frequency depends more strongly on the electron density adopted, less on the electron temperature, and more weakly on the path L . We assume constant electron temperature $T_e = 5000 \text{ K}$ and density $n_e = 2.0 \text{ cm}^{-3}$ (Castelletti et al. 2021).

By adopting these values, our model is calibrated to reproduce an average value $v_* \sim 30 \text{ MHz}$ observed in the combined sample of Castelletti et al. (2021) plus this work, Kovalenko et al. (1994b), and Kassim (1989) (see Fig. 7). The linear length L is computed as the cumulative sum of all segments along the integral that intersect circular ionized clumps of radius r along the line of sight from the solar position. Notice that the NE2001 model cannot predict such characteristic frequencies $v_* \sim 30 \text{ MHz}$ for SNRs that are located nearby (i.e. at heliocentric distances of $\sim 1 \text{ kpc}$) due to the low electron density assumed ($n_e \sim 0.2 \text{ cm}^{-3}$), which is approximately one order of magnitude lower than that inferred from the SNR turnover spectra by Castelletti et al. (2021).

The prediction of our model is shown in Fig. 9, where the spatial distribution of the emitters (SNRs) are plotted as colored dots (using the color coding shown in the upper bar), while the absorbers are displayed as black open circles. To make the plot more clear the scale of each open circle has been expanded by an arbitrary factor of 3. The observer is assumed to be at Cartesian coordinates (0,8.5) kpc from the Galactic centre mimicking the Sun's position. Colored points correspond to SNRs that are absorbed by ionized gas along the line of sights. In a model of sparse and discrete absorbers, like this one, SNRs with

and without spectral turnover are predicted to be mixed, i.e. not spatially segregated as expected in a model with absorbers continuously distributed. In a continuous model, SNRs with non-thermal turnovers are expected to be located closer to the observer while those showing turnovers should exhibit characteristic frequencies v_* increasing with distance. This is because the radiation passes through more gas as it travels towards the observer, leading to increased intersection and thus a higher predicted frequency. Notice that the asymmetric coil of spiral arms, i.e. that its Galacto-centric distance increases with its polar angle, makes absorption asymmetric between the 1st and 4th and between the 2nd and 3rd quadrants. The strongest absorption is predicted in the fourth quadrant tangential direction (see magenta dots) of the most internal spiral arm.

We conducted a series of tests on our model using different values of the scale-length parameter, R_d , for the exponential distribution of SNRs. We also experimented with using a power-law profile, $\Sigma(R) = \Sigma_0(R/R_d)^\gamma$. Despite these changes, we found that our results remained consistent and robust.

To compare observational results against the predictions of our simple model, in Figs. 10 and 11 we plot the characteristic frequency v_* as a function of the heliocentric distance and the Galactic longitude, respectively. Observational values for spectra with turnovers, indicated by colored filled circles (Castelletti et al. 2021 plus this work), small black filled squares (Kovalenko et al. 1994b) and small black filled triangles (Kassim 1989), show neither a positive gradient with distance nor a negative gradient with Galactic longitude, as expected in a model of continuously distributed absorbing gas. Theoretical models fea-

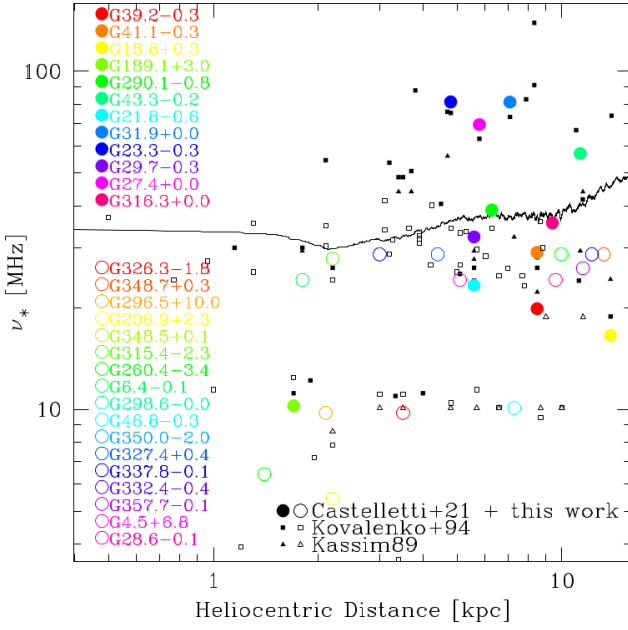


Fig. 10. Characteristic frequency ν_* as a function of the heliocentric distance for SNRs with low frequency turnovers (filled symbols) and SNRs spectra without turnovers (open symbols). Circles correspond to Castelletti et al. (2021) plus this work data, while squares to Kovalenko et al. (1994b), and triangles to Kassim (1989). The solid line corresponds to the median prediction of the model presented in Fig. 9 not showing a systematic gradient with heliocentric distance.

turing discrete absorbers, as depicted in Fig. 9 reveal that the values of ν_* remain approximately constant. This indicates that absorption is independent of heliocentric distance or Galactic longitude, as illustrated by the black continuous solid line. Besides, we have also included observed SNRs with no measured spectral turnovers (i.e. sources with pure power-law continuum spectra) with ν_* computed as the upper limit allowed by the lowest observed frequency ν_{low} (see Sec. 3.2). These remnants are located not only quite close, $d \sim 2$ kpc, to the solar position, but also at distances as large as $d \sim 10$ kpc. Similarly, they can be found either quite close the Galactic center or in the anticenter direction.

Based on our assumed distribution of H II regions following the spiral arms, we find that the absorption of our mock SNR population is consistent with the patchy distribution of absorption indicated by observations to date. A much larger sample of low frequency spectra are needed to verify if our model of absorbing gas due to H II regions is the correct approach.

5. Conclusions

We have analyzed a sample of 129 radio continuum spectra of Galactic SNRs from this work and the literature (including Castelletti et al. 2021, Kovalenko et al. 1994b, and Kassim 1989). 57 show low frequency turnovers characteristic of extrinsic thermal absorption, while 72 remain straight power laws (special cases of intrinsic absorption by unshocked ejecta within SNRs is not considered in this paper). Since the frequencies sampled vary across the spectra, we take care to interpret the latter as limits on absorption in context of their lowest frequency measurement. Our main conclusions are:

1. We introduced a new parametrization of SNR integrated radio continuum spectra in terms of characteristic frequency

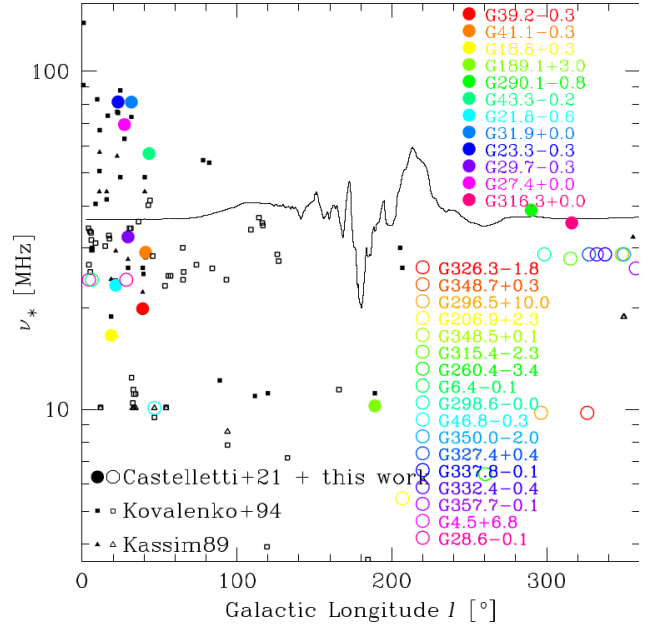


Fig. 11. Characteristic frequency ν_* as a function of the Galactic longitude for SNRs with low frequency turnovers (filled symbols) and SNRs spectra without turnovers (open symbols). Circles correspond to Castelletti et al. (2021) plus this work data, while squares to Kovalenko et al. (1994b), and triangles to Kassim (1989). The solid line corresponds to the median prediction of the model presented in Fig. 9 not showing a strong dependence with the Galactic longitude.

ν_* and corresponding flux density S_* independent of arbitrary survey reference frequencies. ν_* is directly related both to the power-law emission slope and the turnover frequency including the density, temperature, and path through the absorbing medium.

2. Normalizing the SNR spectra to the frequency ν_* and to the flux density S_* , we confirmed with our larger sample that while all SNRs emit energy with independent synchrotron emission power-law indices, turnovers are all well fit by thermal absorption.
3. For SNRs not showing turnovers we derive an upper limit for ν_* by considering the lowest sampled frequency yielding a range of $4 \text{ MHz} \lesssim \nu_* \lesssim 40 \text{ MHz}$. This result should be tested and improved by forthcoming surveys pushing SNR spectra to lower frequencies, especially $< 50 \text{ MHz}$ where sensitivity to absorption is markedly increased.
4. Emission (α) and absorption (ν_*) spectral parameters do not show any significant correlation indicating two unrelated, independent processes. For example, absorption beyond the nominal boundaries of the synchrotron emitting plasma seem oblivious to the details and history of the shock acceleration processes within the remnant. For our three samples of SNR spectra with turnovers we found the characteristic frequency ranges $10 \text{ MHz} \lesssim \nu_* \lesssim 100 \text{ MHz}$.
5. There is no evidence for a correlation between absorption and global Galactic geometric parameters such as heliocentric distance and Galactic longitude, as would be expected if the distribution of the absorbing gas were continuous. Our result is also valid for pure power-law SNR spectra. This is consistent with Kassim (1989) who inferred that SNRs were being absorbed by an intervening patchy distribution of H II regions or their envelopes whose distances were unknown.
6. Modelling based on a distribution of H II regions tracking Galactic spiral arms produces patchy absorption towards a

mock SNR population consistent with the limited observations to date. One prediction of this scheme is that strongly absorbed SNRs should be located preferentially towards the fourth Galactic quadrant relative to the first.

7. Emission measures predicted from NE2001 could not match the observations. We attribute the discrepancy to the fact that the NE2001 model assumes a nearly continuous distribution of ionized gas, and relies predominantly on a relatively nearby population of PSRs. The NE2001 model predicts a correlation between absorption and distance, particularly for greater distances, that is not observed.

Unfortunately, the incompleteness of current SNR catalogs, and absence of low frequency spectra even for those that are known, preclude making a much more detailed comparison between models and observations. This motivates the completion of deeper, global surveys at both MHz and GHz frequencies, to push all SNR spectra to lower frequencies and to fully sample the intrinsic properties like density, temperature, size, and distance, of intervening Galactic thermal gas. Arc-second resolution observations below 100 MHz, as provided by LOFAR and emerging low frequency instruments like LWA and SKA-Low, are critical for discerning the relative radial superposition of SNRs and H II regions along complex lines of sight. Given readily available kinematic distances to H II regions, this can offer powerful physical constraints for SNRs whose distances are far more problematic.

Acknowledgements. This work has been partially supported by the Consejo de Investigaciones Científicas y Técnicas de la República Argentina (CONICET), the Secretaría de Ciencia y Técnica de la Universidad Nacional de Córdoba (SeCyT), Agencia Nacional de Promoción Científica y Tecnológica (PICT 2017-3320, PICT 2019-1600), Argentina. MA acknowledges the hospitality of the Astronomical Observatory of Trieste where part of the work was done in the framework of the European Union LACEGAL program. Basic research in radio astronomy at the Naval Research Laboratory is funded by 6.1 Base funding. Part of this research was carried out at the Jet Propulsion Laboratory, California Institute of Technology, under a contract with the National Aeronautics and Space Administration.

Data availability

The data underlying this article will be shared on reasonable request to the corresponding author.

References

Anantharamaiah, K. R. 1985, *Journal of Astrophysics and Astronomy*, 6, 203
 Anderson, L. D., Armentrout, W. P., Luisi, M., et al. 2018, *ApJS*, 234, 33
 Arias, M., Vink, J., de Gasperin, F., et al. 2018, *A&A*, 612, A110
 Arias, M., Vink, J., Zhou, P., et al. 2019, *AJ*, 158, 253
 Bietenholz, M. F., Kassim, N., Frail, D. A., et al. 1997, *ApJ*, 490, 291
 Blandford, R. & Eichler, D. 1987, *Phys. Rep.*, 154, 1
 Braude, S. I., Megn, A. V., Sokolov, K. P., Tkachenko, A. P., & Sharykin, N. K. 1979, *Ap&SS*, 64, 73
 Braude, S. Y., Lebedeva, O. M., Megn, A. V., Ryabov, B. P., & Zhouck, I. N. 1969, *MNRAS*, 143, 289
 Bridle, A. H. & Purton, C. R. 1968, *AJ*, 73, 717
 Brogan, C. L., Lazio, T. J., Kassim, N. E., & Dyer, K. K. 2005, *AJ*, 130, 148
 Carretti, E., Haverkorn, M., Staveley-Smith, L., et al. 2019, *MNRAS*, 489, 2330
 Castelletti, G., Supan, L., Peters, W. M., & Kassim, N. E. 2021, *A&A*, 653, A62
 Cordes, J. M. & Lazio, T. J. W. 2002, *arXiv e-prints*, astro
 DeLaney, T., Kassim, N. E., Rudnick, L., & Perley, R. A. 2014, *ApJ*, 785, 7
 Dulk, G. A. & Slee, O. B. 1975, *ApJ*, 199, 61
 Dulk, P. & Slee, O. 1972, *Australian Journal of Physics*, 25, 429
 Erickson, W. C. & Cronyn, W. M. 1965, *ApJ*, 142, 1156
 Haynes, R. F., Caswell, J. L., & Simons, L. W. J. 1978, *Australian Journal of Physics Astrophysical Supplement*, 45, 1
 Hou, L. G. & Han, J. L. 2014, *A&A*, 569, A125

Hurley-Walker, N., Hancock, P. J., Franzen, T. M. O., et al. 2019, *PASA*, 36, e047
 Jones, B. B. & Finlay, E. A. 1974, *Australian Journal of Physics*, 27, 687
 Kassim, N. E. 1988, *ApJS*, 68, 715
 Kassim, N. E. 1989, *ApJ*, 347, 915
 Kassim, N. E., Perley, R. A., Dwarakanath, K. S., & Erickson, W. C. 1995, *ApJ*, 455, L59
 Kovalenko, A. V., Pynzar', A. V., & Udal'Tsov, V. A. 1994a, *AZh*, 71, 110
 Kovalenko, A. V., Pynzar', A. V., & Udal'Tsov, V. A. 1994b, *Astronomy Reports*, 38, 78
 Lacey, C. K., Lazio, T. J. W., Kassim, N. E., et al. 2001, *ApJ*, 559, 954
 Lane, W. M., Clarke, T. E., Taylor, G. B., Perley, R. A., & Kassim, N. E. 2004, *AJ*, 127, 48
 Malkov, M. A. & Drury, L. O. 2001, *Reports on Progress in Physics*, 64, 429
 McClure-Griffiths, N. M., Dickey, J. M., Gaensler, B. M., et al. 2005, *ApJS*, 158, 178
 Mills, B. Y. & Slee, O. B. 1957, *Australian Journal of Physics*, 10, 162
 Mills, B. Y., Slee, O. B., & Hill, E. R. 1958, *Australian Journal of Physics*, 11, 360
 Mills, B. Y., Slee, O. B., & Hill, E. R. 1960, *Australian Journal of Physics*, 13, 676
 Ranasinghe, S. & Leahy, D. 2022, *ApJ*, 940, 63
 Rishbeth, H. 1958, *Australian Journal of Physics*, 11, 550
 Roger, R. S., Costain, C. H., & Lacey, J. D. 1969, *AJ*, 74, 366
 Roger, R. S., Costain, C. H., & Stewart, D. I. 1986, *A&AS*, 65, 485
 Slee, O. B. 1977, *Australian Journal of Physics Astrophysical Supplement*, 43, 1
 Slee, O. B. & Higgins, C. S. 1973, *Australian Journal of Physics Astrophysical Supplement*, 27, 1
 Slee, O. B. & Higgins, C. S. 1975, *Australian Journal of Physics Astrophysical Supplement*, 36, 1
 Viner, M. R. & Erickson, W. C. 1975, *AJ*, 80, 931
 Wenger, T. V., Dawson, J. R., Dickey, J. M., et al. 2021, *ApJS*, 254, 36
 Williams, P. J. S., Kenderdine, S., & Baldwin, J. E. 1966, *MmRAS*, 70, 53
 Wilson, T. L., Rohlf, K., & Hüttemeister, S. 2009, *Tools of Radio Astronomy*

Appendix A: Fitted parameters of SNRs spectra sample

Table A.1. Each group of rows, separated by a horizontal line, corresponds to Castelletti et al. (2021) and this work data, Kovalenko et al. (1994b), and Kassim (1989) sample, respectively. Column 1 is the SNR identification name while columns 2 to 6 are published parameter for Eq. 1 taken from these references. For SNRs G189.1+3.0, G290.1−0.8, and G316.3+0.0, we derived the parameters through spectral fits to the datasets constructed for this study. Column 7 and 8 display our computed values for ν_* and S_* , respectively, using $\nu_* = \tau_0^{1/2.1} \nu_0$ and $S_* = S_1(\nu_*/\nu_1)^\alpha$ (see Eq. 2).

SNR	α	ν_0 [MHz]	τ_0	ν_1 [MHz]	S_1 [Jy]	ν_* [MHz]	S_* [Jy]
G18.8+0.3 (Kes 67)	−0.373	74	0.043	74	79.75	16.54	139.46
G21.8−0.6 (Kes 69)	−0.505	74	0.088	74	208.00	23.26	373.16
G23.3−0.3 (W41)	−0.628	74	1.214	74	347.20	81.16	327.62
G27.4+0.0 (Kes 73)	−0.690	74	0.878	74	34.72	69.55	36.24
G29.7−0.3 (Kes 75)	−0.659	74	0.176	74	50.87	32.36	87.74
G31.9+0.0 (3C 391)	−0.521	74	1.210	74	90.70	81.03	86.51
G39.2−0.3 (3C 396)	−0.351	74	0.063	74	41.65	19.84	66.11
G41.1−0.3 (3C 397)	−0.356	74	0.141	74	75.30	29.11	104.96
G43.3−0.2 (W49B)	−0.461	74	0.580	74	111.80	57.09	125.96
G189.1+3.0 (IC 443)	−0.388	74	0.016	74	436.90	10.24	941.26
G290.1−0.8 (MSH 11−61A)	−0.421	74	0.258	74	137.80	38.82	180.80
G316.3+0.0	−0.893	74	0.215	74	166.20	35.59	319.52
G0.9+0.1	−0.64	100	0.820	2000	6.9	90.98	49.86
G1.05−0.1	−0.66	100	2.000	1700	13.0	139.10	67.83
G6.4−0.1 (W28)	−0.42	100	0.080	450	440.0	30.04	1371.00
G8.7−0.1 (W30)	−0.48	100	0.150	940	80.0	40.52	361.80
G9.8+0.6	−0.56	100	0.670	740	4.1	82.64	13.99
G11.2−0.3	−0.49	100	0.240	6000	9.2	50.68	95.43
G11.4−0.1	−0.46	100	0.430	1000	6.0	66.91	20.82
G15.9+0.2	−0.63	100	0.160	1100	4.2	41.78	32.97
G16.7+0.1	−0.53	100	0.530	960	2.9	73.91	11.29
G18.8+0.3 (Kes 67)	−0.42	100	0.030	580	37.0	18.83	156.10
G20.0−0.2	−0.00	100	0.05	180	10.0	24.01	10.00
G21.8−0.6 (Kes 69)	−0.50	100	0.050	600	77.0	24.01	384.90
G22.7−0.2	−0.40	100	0.560	1850	59.0	75.87	211.70
G23.3−0.3 (W41)	−0.48	100	0.550	190	190.0	75.23	296.40
G24.7−0.6	−0.59	100	0.760	800	8.0	87.75	29.47
G24.7+0.6	−0.14	100	0.220	1600	18.0	48.63	29.36
G27.4+0.0	−0.71	100	0.380	560	9.4	63.08	44.30
G29.7−0.3 (Kes 75)	−0.59	100	0.060	3100	4.4	26.19	73.56
G31.9+0.0 (3C 391)	−0.51	100	0.520	2200	15.5	73.24	87.89
G39.2−0.3 (3C 396)	−0.48	100	0.060	840	20.0	26.19	105.70
G39.7−2.0 (W50)	−0.50	100	0.055	760	90.0	25.13	495.00
G40.5−0.5	−0.51	100	0.220	410	19.5	48.63	57.84
G41.1−0.3 (3C 397)	−0.46	100	0.070	10000	7.0	28.19	104.30
G78.2+2.1 (γ -Cygni)	−0.73	100	0.280	1480	40.0	54.54	2671.00
G82.2+5.3 (W63)	−0.63	100	0.270	1900	73.0	53.61	691.10
G89.0+4.7 (HB21)	−0.39	100	0.012	800	240.0	12.17	1228.00
G111.7−2.1	−0.75	100	0.010	180	11500.0	10.94	93922.52
G120.1+1.4	−0.62	100	0.010	520	86.0	11.16	930.89
G189.1.1−3.0	−0.42	100	0.010	700	190.0	11.16	1080.67
G205.5+0.5 (Monoceros)	−0.47	100	0.080	1300	135.0	30.04	793.20
G206.9+2.3 (PKS 0646+06)	−0.51	100	0.060	360	10.0	26.19	38.06
G6.4−0.1 (W28)	−0.4	30.9	0.9	408	424.0	29.39	1214.00
G11.2−0.3	−0.5	30.9	2.1	408	30.0	43.99	91.36
G11.4−0.1	−0.4	30.9	3.7	408	7.1	57.61	15.53
G15.9+0.2	−0.7	30.9	2.1	408	8.5	43.99	40.41
G18.8+0.3 (Kes 67)	−0.5	30.9	0.6	408	49.0	24.23	201.10
G21.8−0.6 (Kes 69)	−0.5	30.9	0.9	408	95.0	29.39	354.00
G22.7−0.2	−0.2	30.9	3.5	408	65.0	56.11	96.66
G23.3−0.3 (W41)	−0.4	30.9	7.2	408	119.0	79.11	229.40
G29.7−0.3 (Kes 75)	−0.6	30.9	0.8	408	15.0	27.79	75.20
G39.2−0.3 (3C 396)	−0.4	30.9	0.5	408	25.0	22.21	80.09
G40.5−0.5	−0.5	30.9	2.1	408	16.0	43.99	48.73
G41.1−0.3 (3C 397)	−0.4	30.9	0.9	408	39.0	29.39	111.70
G43.3−0.2 (W49)	−0.4	30.9	0.9	408	46.0	29.39	131.80
G355.9−2.5	−0.5	30.9	1.1	408	12.0	32.33	42.63